Numerical Investigation of Stall Flutter in a Pitching Airfoil at Low Reynolds Number

Maria Adele Cecchini , Giulio Soldati , Peter Jordan , Sergio Pirozzoli *

Posted Date: 21 May 2026

doi: 10.20944/preprints202605.1300.v1

Keywords: stall flutter; aeroelastic response; frequency analysis

 doi:10.20944/preprints202605.1300.v1

Article

Numerical Investigation of Stall Flutter in a Pitching Airfoil at Low Reynolds Number

Maria Adele Cecchini [1], Giulio Soldati [1], Peter Jordan [2] and Sergio Pirozzoli [1,*]

[1] Dipartimento di Ingegneria Meccanica e Aerospaziale, Sapienza Università di Roma, Via Eudossiana 18, 00184 Roma, Italy
[2] Département Fluides, Thermique et Combustion, Université de Poitiers, 86360 Futuroscope-Chasseneuil, France
* Correspondence: sergio.pirozzoli@uniroma1.it

Abstract

The present work investigates fluid—structure instabilities and stall flutter of a pitching NACA0012 airfoil through numerical simulations. The flow is modeled using the compressible Navier—Stokes equations in a non-inertial rotating reference frame, while the structural dynamics are represented by a torsional spring—mass—damper system. The analysis focuses on the effects of reduced velocity, equilibrium angle of attack, and elastic axis position on the aeroelastic behavior. The results show a transition from steady flow to vortex-shedding regimes and, at higher reduced velocities, to limit-cycle oscillations. Increasing the equilibrium angle of attack leads to an earlier onset of instability and stronger aerodynamic forcing, while moving the elastic axis downstream has a similar destabilizing effect due to the larger aerodynamic moment arm. Frequency analysis highlights the progressive coupling between fluid and structural dynamics: vortex shedding dominates at low reduced velocity, whereas the structural frequency governs the response in the limit-cycle regime. The study provides a consistent description of the mechanisms driving stall flutter and of the parameters influencing aeroelastic stability.

Keywords: stall flutter; aeroelastic response; frequency analysis

1. Introduction

Fluid–structure interaction (FSI) phenomena arise in a wide range of natural and engineering systems, where the coupling between aerodynamic loads and structural dynamics can lead to complex and potentially unstable behaviour. In aeronautical applications, aeroelastic instabilities such as flutter represent a critical design constraint, as they may compromise structural integrity and must be avoided within the operational envelope [1]. At the same time, controlled fluid–structure coupling is increasingly exploited in modern configurations, including flexible and morphing wings, where aeroelastic effects can enhance aerodynamic performance.

Flutter is fundamentally governed by the interaction between unsteady aerodynamic forces and structural dynamics. In its simplest form, the problem can be interpreted as a competition between structural and flow time scales [2]. The structural response is characterized by its natural frequency and damping, while the flow introduces additional time scales associated with separation, vortex formation, and reattachment. Their interaction may lead to self-sustained oscillations when the aerodynamic energy input overcomes structural dissipation.

At low Reynolds numbers, the role of flow separation and dynamic stall becomes particularly important, leading to strongly nonlinear behaviour. In these regimes, the aeroelastic response is often characterized by large-amplitude limit-cycle oscillations (LCO), hysteresis, and complex bifurcation structures that cannot be described by linear theory. Understanding the mechanisms governing these regimes is therefore essential for predicting and controlling aeroelastic instabilities.

The unsteady aerodynamics of pitching airfoils under prescribed motion has been extensively investigated to characterize separation dynamics and vortex evolution. It has been shown that the

 doi:10.20944/preprints202605.1300.v1

development of boundary layer separation depends sensitively on reduced frequency [3], while Reynolds number effects significantly influence aerodynamic loads [4]. More recent studies have further clarified the reattachment process in dynamic stall conditions, highlighting the presence of multiple temporal stages [5].

In parallel, flow-induced oscillations of elastically supported airfoils have been widely studied using simplified configurations, typically consisting of a rigid airfoil mounted on a torsional spring–damper system. Despite their apparent simplicity, such systems exhibit rich nonlinear dynamics. Experimental investigations have reported self-sustained oscillations at transitional Reynolds numbers [6], while cyber-physical experiments and numerical studies have demonstrated the strong sensitivity of the aeroelastic response to both structural and aerodynamic parameters [7,8].

A common interpretation emerging from these studies is that flutter can be described in terms of energy exchange between the fluid and the structure. Oscillations grow when the net aerodynamic work over one cycle exceeds structural dissipation, and saturate when the two contributions balance. This perspective has been formalized through energy-based approaches, including the concept of energy maps for forced oscillations [2], and more recent extensions to stall flutter prediction and control [9,10].

In this work, we investigate flow-induced pitch oscillations of a rigid NACA0012 airfoil elastically supported by a linear torsional spring and damper. The analysis is conducted at low Reynolds number ($Re = 1000$), where nonlinear flow phenomena can be examined in detail. The coupled fluid–structure system is solved numerically using the compressible Navier–Stokes equations formulated in a rotating reference frame, together with a single-degree-of-freedom structural model. After verification and validation of the numerical framework, we focus on the influence of reduced velocity, equilibrium angle of attack, and elastic axis position on the aeroelastic response. The objective is to identify the parameters controlling flutter onset, oscillation amplitude, and frequency characteristics, and to characterize the transition from vortex-shedding-dominated behaviour to fully coupled aeroelastic regimes. Although the present study is restricted to low Reynolds numbers, the results provide insight into the fundamental mechanisms governing stall flutter and fluid–structure coupling, which are relevant to more complex aeroelastic systems.

2. Problem Setup

We consider a two-dimensional NACA0012 airfoil immersed in a uniform flow of free-stream velocity u_0. The airfoil is allowed to rotate about a prescribed elastic axis and is analyzed within a non-inertial reference frame rigidly attached to the body, as schematically shown in Figure 1. This formulation allows the airfoil to remain fixed in the computational domain, while its motion is accounted for through additional source terms in the governing equations.

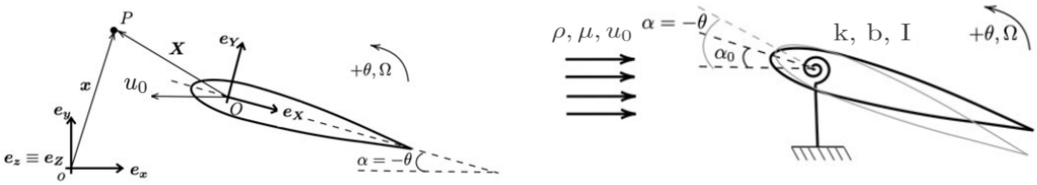

Figure 1. Schematic of the problem configuration. Left: non-inertial reference frame (e_X, e_Y) rigidly attached to the airfoil and rotating with angular velocity $\mathbf{\Omega}$ with respect to the inertial frame (e_x, e_y). Right: airfoil elastically supported by a torsional spring–damper system with inertia I, stiffness k, and damping b, allowed to rotate about an elastic axis located at X^*_{ec} around the equilibrium angular position α_0. The airfoil is immersed in a uniform flow of density ρ and viscosity μ, with free-stream velocity u_0.

 doi:10.20944/preprints202605.1300.v1

The aerodynamic field is described by the compressible Navier–Stokes equations expressed in the rotating frame. In terms of relative variables, the conservation of mass reads

$$\frac{\partial \hat{\rho}}{\partial t} + \nabla \cdot (\hat{\rho}\hat{\boldsymbol{u}}) = 0, \tag{1}$$

where the hat symbol denotes the quantities in the rotating frame.

The momentum equation is written as

$$\frac{\partial (\hat{\rho}\hat{\boldsymbol{u}})}{\partial t} = -\nabla \cdot (\hat{\rho}\hat{\boldsymbol{u}} \otimes \hat{\boldsymbol{u}}) - \nabla \hat{p} + \nabla \cdot \hat{\boldsymbol{\sigma}} + 2\hat{\rho}\hat{\boldsymbol{u}} \times \boldsymbol{\Omega} - \hat{\rho}\boldsymbol{\Omega} \times (\boldsymbol{\Omega} \times \hat{\boldsymbol{x}}) + \hat{\rho}\dot{\boldsymbol{\Omega}} \times \hat{\boldsymbol{x}}, \tag{2}$$

where $\boldsymbol{\Omega}$ is the angular velocity vector and $\hat{\boldsymbol{x}}$ the position vector. The additional terms represent the Coriolis, centrifugal, and Euler forces arising from the non-inertial formulation. The viscous stress tensor is defined as

$$\hat{\boldsymbol{\sigma}} = \hat{\mu}\left(\nabla \hat{\boldsymbol{u}} + \nabla \hat{\boldsymbol{u}}^T\right) - \frac{2}{3}\hat{\mu}(\nabla \cdot \hat{\boldsymbol{u}})\boldsymbol{I}. \tag{3}$$

The total energy equation reads

$$\frac{\partial (\hat{\rho}\hat{E})}{\partial t} = -\nabla \cdot (\hat{\rho}\hat{\boldsymbol{u}}\hat{H}) + \nabla \cdot (\hat{\boldsymbol{\sigma}} \cdot \hat{\boldsymbol{u}}) - \nabla \cdot \hat{\boldsymbol{q}} + \boldsymbol{f}_{\text{rot}} \cdot \hat{\boldsymbol{u}}, \tag{4}$$

where $\hat{\boldsymbol{q}} = -\hat{k}\nabla \hat{T}$ and $\boldsymbol{f}_{\text{rot}} \cdot \hat{\boldsymbol{u}}$ is the power density of non-inertial forces.

The velocity in the rotating frame is related to the absolute velocity through

$$\hat{\boldsymbol{u}} = \boldsymbol{u} - \boldsymbol{\Omega} \times \boldsymbol{r}. \tag{5}$$

The system is closed using the perfect gas law and Sutherland's law for viscosity. The airfoil is elastically supported by a torsional spring–damper system, providing a single rotational degree of freedom, as illustrated in Figure 1. The structural dynamics are governed by

$$I^*\ddot{\alpha} + b^*\dot{\alpha} + k^*(\alpha - \alpha_0) = C_M, \tag{6}$$

where I^*, b^*, and k^* are the non-dimensional inertia, damping, and stiffness coefficients, C_M is the aerodynamic moment coefficient, $\alpha = -\theta$ is the angle of attack, and α_0 is the equilibrium angular position of the airfoil. The damping is also expressed through the non-dimensional damping ratio

$$\zeta^* = \frac{b}{2\sqrt{kI}}. \tag{7}$$

The aeroelastic response is characterized by the reduced velocity

$$U^* = \frac{u_0}{f_n c}, \tag{8}$$

and the natural frequency

$$f_n = \frac{1}{2\pi}\sqrt{\frac{k}{I}}. \tag{9}$$

The coupled fluid–structure system is obtained by solving the flow equations together with the structural dynamics, where the aerodynamic moment acts as the forcing term driving the airfoil motion.

3. Numerical Method

The governing equations are discretised using a finite volume method on a structured body-fitted grid. The conservative form of the compressible Navier–Stokes equations is integrated over each control volume. Convective fluxes are evaluated using a central differencing scheme, stabilised through

 doi:10.20944/preprints202605.1300.v1

the triple-splitting form proposed by Pirozzoli [11,12], Soldati et al. [13], such that the overall kinetic energy of the fluid is discretely preserved in the limit of inviscid, incompressible flow. Viscous fluxes are discretised using second-order central differences. Time integration is performed using an explicit third-order Runge–Kutta scheme, which provides efficient convergence to the solution. The source terms associated with the rotating reference frame are explicitly included in the residual evaluation, ensuring consistency between the flow solution and the airfoil motion.

Boundary conditions are defined consistently with the rotating reference frame formulation. At the airfoil surface, a no-slip condition is enforced, corresponding to zero relative velocity in the rotating frame. At the far-field boundaries, free-stream conditions are imposed using velocity components expressed in the rotating frame. To avoid spurious reflections at the outer boundaries, a sponge layer is introduced in the far-field region. Within this region, the flow variables are gradually relaxed toward free-stream conditions through a spatially varying damping coefficient. The damping intensity increases smoothly with the radial distance from the airfoil, ensuring a continuous transition between the inner computational domain and the outer boundary.

The computational domain is discretised using a structured C-type mesh around the airfoil, as shown in Figure 2. This configuration allows accurate resolution of the boundary layer along the airfoil surface and an appropriate representation of the wake region.

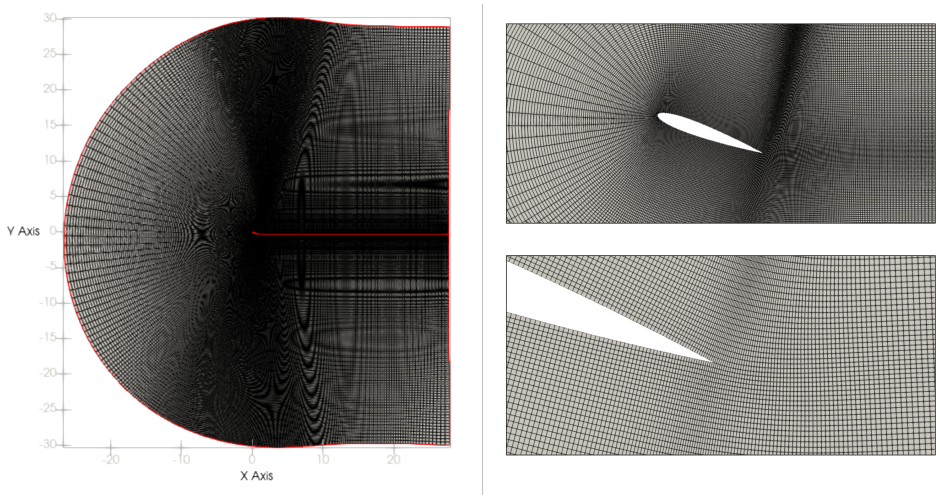

Figure 2. Computational grid. Left: global view of the two-dimensional computational domain. Right: detailed views near the airfoil (top) and near the trailing edge (bottom).

The grid is generated by rotating the airfoil geometry according to the prescribed equilibrium angle of attack (α_0), ensuring alignment between the mesh and the flow configuration. Grid spacing is refined near the airfoil surface to resolve boundary layer gradients, while a gradual coarsening is applied in the far-field and wake regions according to a geometric progression to reduce computational cost. The overall resolution is selected to ensure a balance between accuracy and efficiency, while maintaining smooth grid transitions and avoiding excessive stretching ratios.

4. Verification and Validation

A grid convergence study is performed to assess the sensitivity of the solution to spatial resolution. Three structured grids of increasing resolution are considered, and the resulting time histories of the angle of attack and lift coefficient are compared. Notice that all the time series plot in this study are function of the dimensionless time $t^* = (t - t_0)\ u_0/c$ in order to exclude the transient time interval.

As shown in Figure 3, the intermediate grid provides a solution that is essentially indistinguishable from the finer grid, while significantly reducing the computational cost. This grid is therefore adopted for all subsequent simulations.

 doi:10.20944/preprints202605.1300.v1

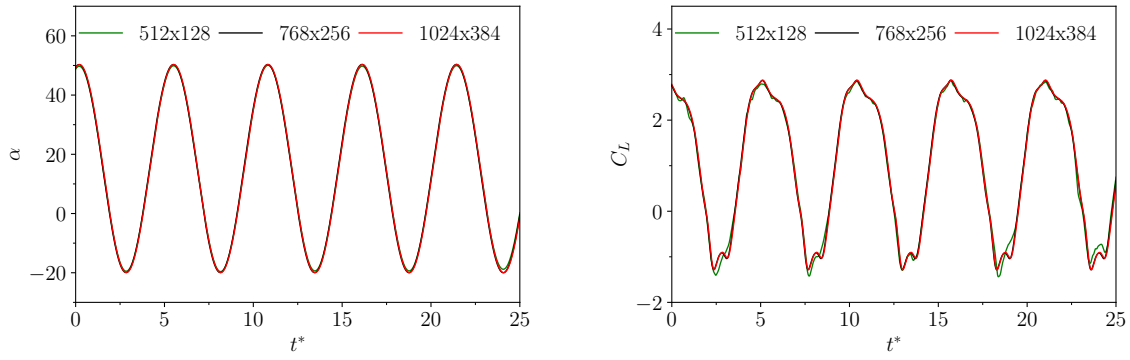

(**a**) (**b**)

Figure 3. Time evolution of the angle of attack (a) and lift coefficient (b) obtained using three grids of increasing resolution.

The correctness of the structural model implementation is verified by considering the case without aerodynamic forcing, for which an analytical solution is available. In this limit, the governing equation reduces to a damped harmonic oscillator.

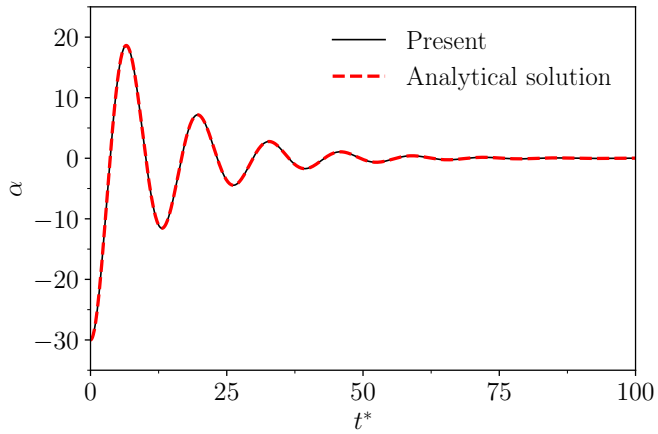

Figure 4. Time evolution of the angle of attack for the unforced structural response obtained from the numerical simulation and compared with the analytical solution.

The numerical results are in perfect agreement with the analytical solution, as shown in Figure 4, thereby confirming the correct implementation of the structural dynamics.

Regarding the flow-induced dynamics, a comparison is carried out with the results obtained by Xia et al. [9] for the case with $\zeta^* = 0.03$, $X_{ec}{}^* = 0.5$, $I^* = 4.5$, $Re = 1000$, $M = 0.1$, and $U^* = 6$. As shown in Figure 5, the present results are in good agreement with those reported in the reference paper.

The numerical results reproduce both the amplitude and temporal evolution of the oscillations with good accuracy, demonstrating the capability of the solver to capture the coupled aeroelastic dynamics.

 doi:10.20944/preprints202605.1300.v1

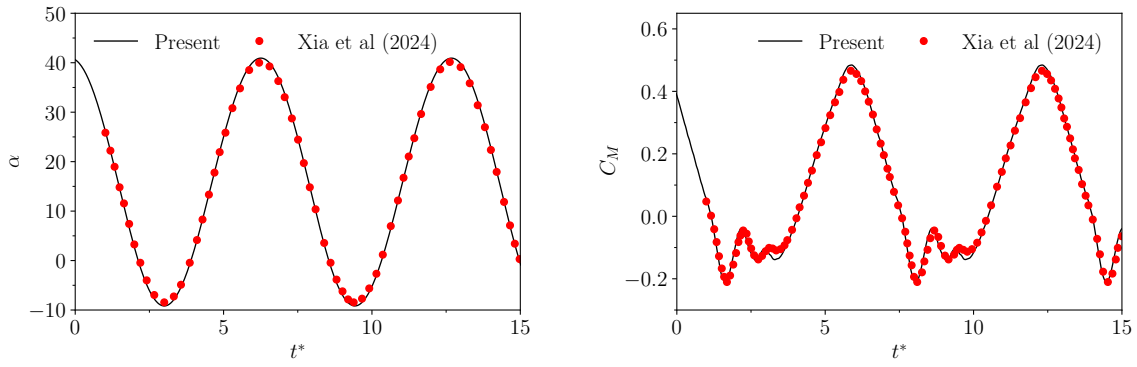

(**a**) (**b**)

Figure 5. Time evolution of the angle of attack (a) and moment coefficient (b) obtained from the numerical simulation and compared with the results reported by Xia et al. [9].

5. Results

5.1. Flow Regimes for the Rigid Airfoil

The aerodynamic response of the rigid airfoil is first analyzed in order to characterize the baseline flow behaviour in the absence of structural coupling. Three equilibrium angles of attack are considered, namely $\alpha_0 = 0°$, 15°, and 30°.

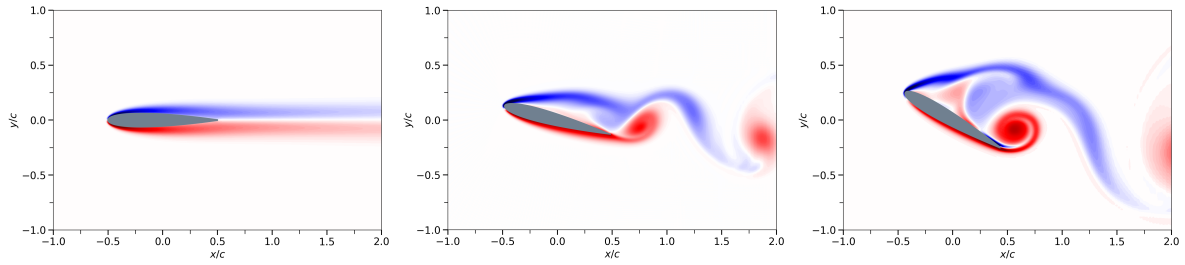

(**a**) (**b**) (**c**)

Figure 6. Instantaneous vorticity fields for increasing equilibrium angles of attack: (a) $\alpha_0 = 0°$, (b) $\alpha_0 = 15°$, and (c) $\alpha_0 = 30°$.

As shown in Figure 6, the flow undergoes a clear transition with increasing the equilibrium angle of attack. At $\alpha_0 = 0°$, the flow remains steady and symmetric, with no evidence of vortex shedding. At $\alpha_0 = 15°$, periodic vortex shedding develops, associated with a coherent separated shear layer. At $\alpha_0 = 30°$, the flow becomes strongly separated and exhibits more complex and irregular vortex dynamics, indicative of a nonlinear regime.

This transition is further quantified through frequency analysis of the aerodynamic loads. The frequency response is expressed in terms of the Strouhal number, $St = fc/u_0$, where f is the dominant frequency extracted from the signals of C_M and C_L. Figures 8 and 7 shows the corresponding time histories and power spectral densities.

At $\alpha_0 = 0°$, no dominant frequency is observed, confirming the steady nature of the flow. For $\alpha_0 = 15°$, a clear peak appears at a characteristic Strouhal number corresponding to periodic vortex shedding. Besides this fundamental frequency, higher harmonics appear indicating a tonal response. At $\alpha_0 = 30°$, the fundamental frequency shifts to a lower value. Multiple peaks are present, reflecting the coexistence of several interacting flow scales and the onset of nonlinear dynamics.

These results identify three distinct flow regimes: a steady regime at low equilibrium angle of attack, a periodic vortex-shedding regime at intermediate angles, and a strongly nonlinear separated

 doi:10.20944/preprints202605.1300.v1

regime at high angles. These baseline behaviours provide the reference framework for interpreting the aeroelastic response of the coupled system.

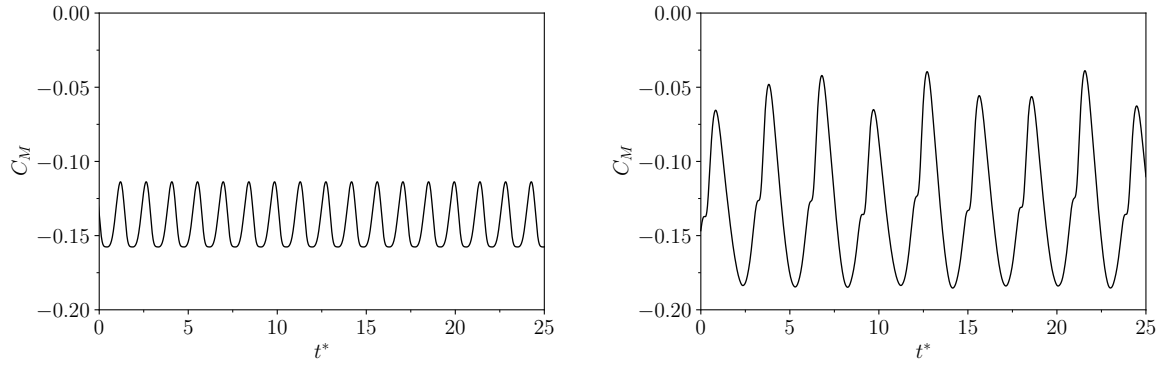

(a) **(b)**

Figure 7. Time evolution of the aerodynamic moment coefficient using a common y-axis for two equilibrium angles of attack: (a) $\alpha_0 = 15°$ and (b) $\alpha_0 = 30°$.

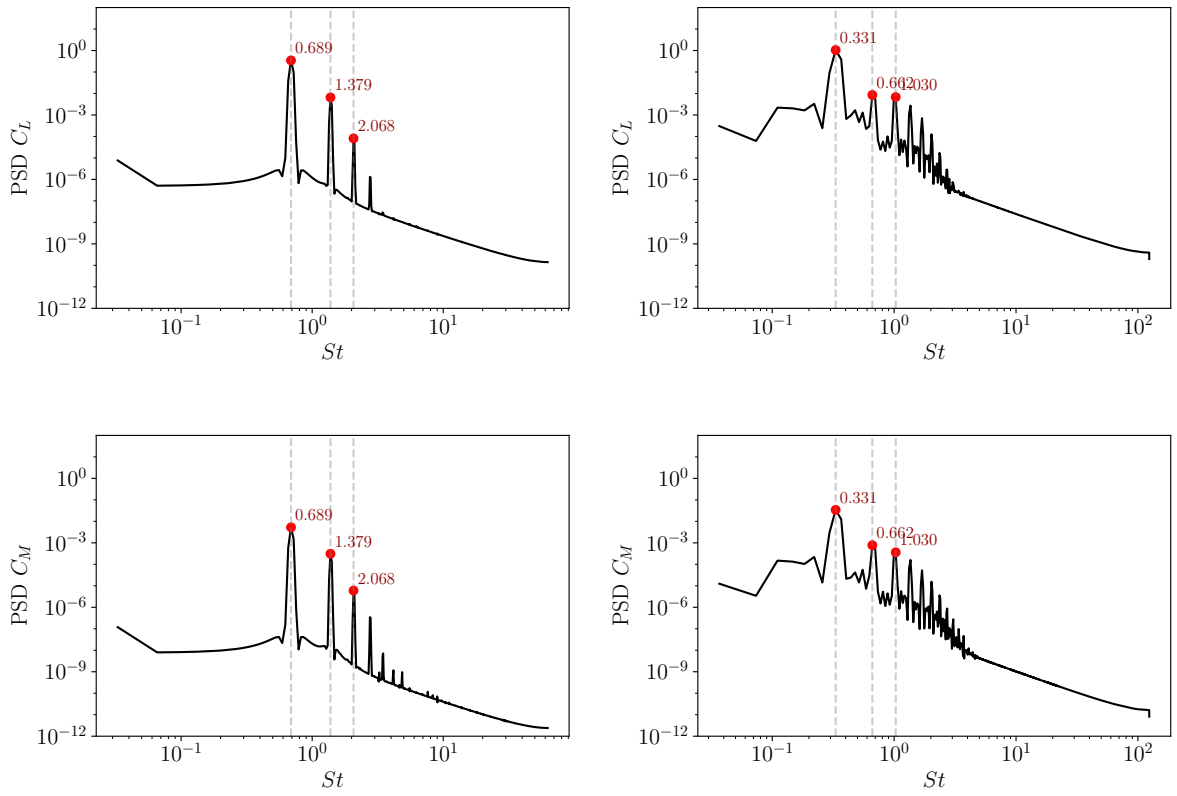

Figure 8. Power spectral density of the lift coefficient (top row) and moment coefficient (bottom row) as a function of the Strouhal number for the rigid airfoil at two equilibrium angles of attack: $\alpha_0 = 15°$ (left column) and $\alpha_0 = 30°$ (right column).

5.2. Flutter Onset and Amplitude Response

The aeroelastic response of the system is investigated as a function of the reduced velocity U^* for different equilibrium angles of attack. The analysis focuses on the evolution of the oscillation amplitude and the identification of the transition to large-amplitude limit-cycle oscillations.

 doi:10.20944/preprints202605.1300.v1

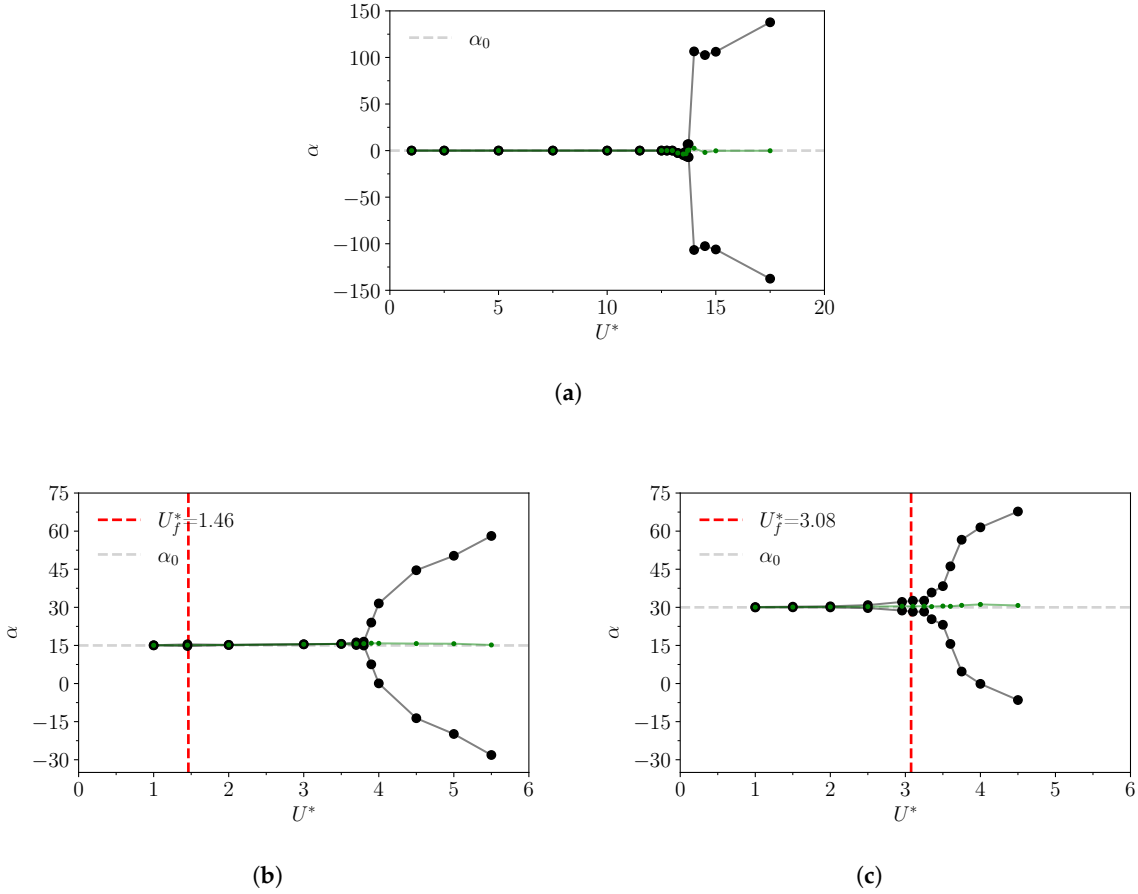

Figure 9. Maximum, minimum, and mean values of the angle of attack as a function of the reduced velocity U^* for different equilibrium angles of attack: $\alpha_0 = 0°$ (a), $\alpha_0 = 15°$ (b), and $\alpha_0 = 30°$ (c). The gray dashed line indicates the equilibrium angle of attack, while the red dashed line denotes the reduced velocity corresponding to the Strouhal-number peak of the associated rigid-airfoil case. The black lines represent the maximum and minimum values of the angle of attack, and the green line denotes the mean value.

Figure 9 shows that the system exhibits a transition from small-amplitude oscillations to large-amplitude motion as the reduced velocity increases. The critical value of U^* at which this transition occurs depends strongly on the equilibrium angle of attack. For $\alpha_0 = 0°$, the system remains essentially stable over a wide range of reduced velocity, and a sudden transition to large oscillations is observed at a critical threshold. This behaviour is characteristic of a subcritical bifurcation, where the instability appears abruptly once a sufficient level of aerodynamic forcing is reached. A subcritcal Hopf bifurcation at $\alpha_0 = 0°$ was consistently observed by Dimitriadis and Li [14] and Onoue et al. [7]. In contrast, for $\alpha_0 = 15°$ and $30°$, the oscillation amplitude increases progressively with U^*, starting from small values and smoothly growing into the limit-cycle regime. This behaviour is indicative of a supercritical bifurcation, associated with the presence of flow separation and vortex shedding already at moderate amplitudes.

The equilibrium angle of attack therefore plays a key role in determining both the onset of flutter and the nature of the transition. Higher values of α_0 lead to an earlier onset of instability, reflecting the stronger aerodynamic forcing associated with separated flow conditions. In addition, the results show that the mean position of the oscillation deviate slightly from the imposed equilibrium angle at low amplitudes, indicating that limit-cycle oscillations are asymmetric [7]. This behaviour reflects a shift of the mean aerodynamic state prior to the onset of fully developed limit-cycle oscillations.

Overall, the system exhibits two distinct transition mechanisms: a subcritical transition at low equilibrium angle of attack and a supercritical transition when separation effects become dominant.

 doi:10.20944/preprints202605.1300.v1

This difference in the bifurcation topology highlights the importance of nonlinear aerodynamic effects in governing stall flutter onset.

5.3. Frequency Coupling and Synchronization

Further insight into the aeroelastic dynamics is obtained by analyzing the frequency content of the response as a function of reduced velocity. The dominant frequencies of the pitch motion and of the aerodynamic moment are extracted and expressed in terms of the Strouhal number (St_p and St_M, respectively).

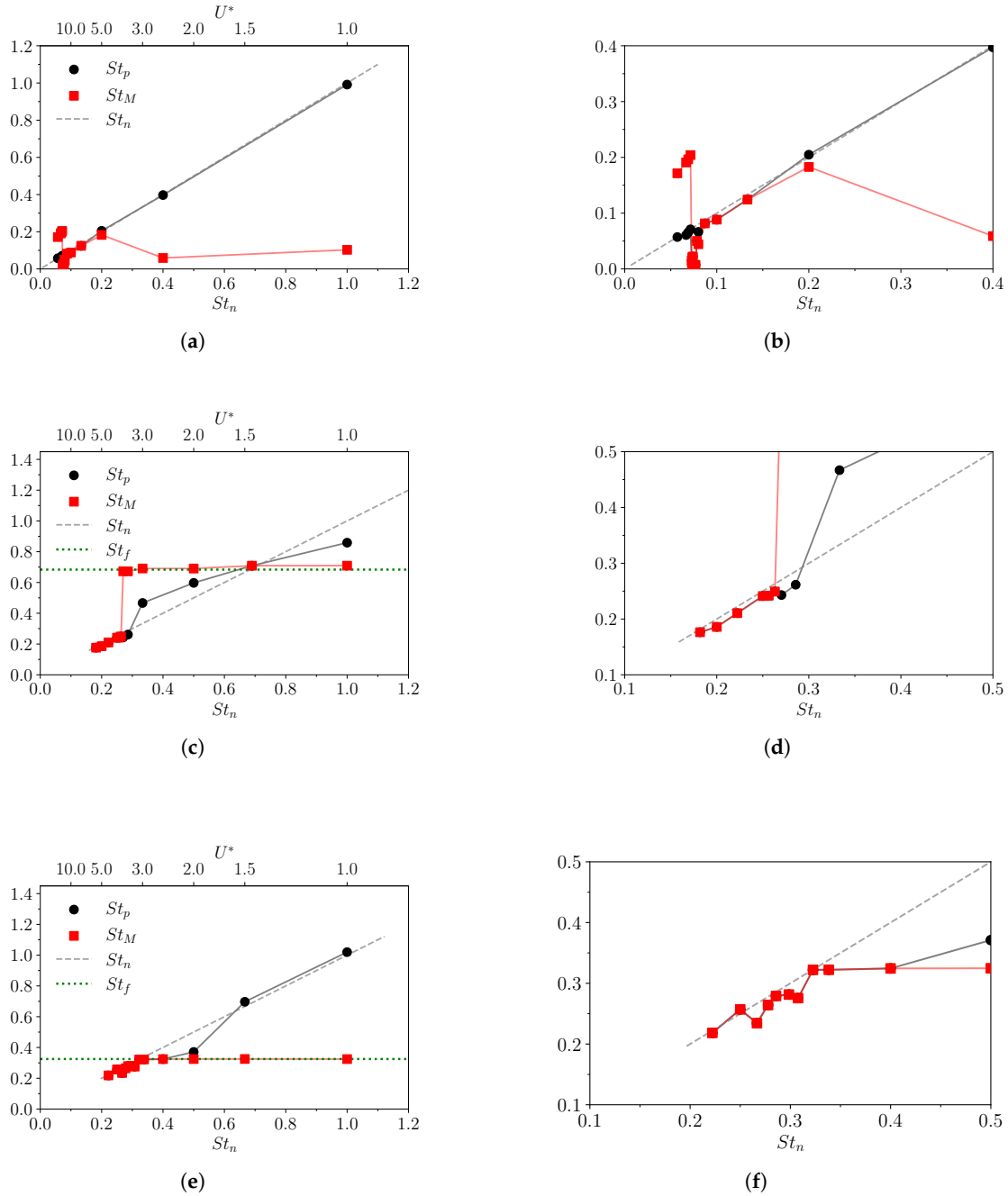

Figure 10. Peak Strouhal numbers as a function of the natural Strouhal number for different equilibrium angles of attack: $\alpha_0 = 0°$ (top row), $\alpha_0 = 15°$ (middle row), and $\alpha_0 = 30°$ (bottom row). The left column shows the full frequency range, while the right column shows a zoom at low frequencies. The black line denotes the Strouhal number associated with the angle of attack, and the red line the Strouhal number associated with the moment coefficient. The gray dotted line indicates the natural Strouhal number, while the green dotted line denotes the Strouhal-number peak value for the corresponding rigid-airfoil case.

 doi:10.20944/preprints202605.1300.v1

Figure 10 shows a clear transition in the frequency response as the reduced velocity increases. Overall, at low U^* (high frequencies), the dominant frequency St_M remains nearly constant and corresponds to the vortex-shedding frequency of the rigid airfoil. In this regime, the structural motion is passively driven by the flow; the coupling between fluid and structure is weak and pitching oscillations occur approximately at the natural frequency St_n. As U^* increases, an intermediate regime is observed in which multiple frequency components coexist. In addition to the vortex-shedding frequency, a lower frequency associated with the structural dynamics emerges. This regime reflects a partial coupling between fluid and structure, where both mechanisms contribute to the response. At sufficiently large U^*, the system transitions to a regime in which both St_M and St_p collapse into a single dominant frequency corresponding to the natural frequency of the structure. In this limit-cycle regime, the aerodynamic loads and structural motion become synchronized, and the dynamics are governed by the structural response.

As highlighted in the zoomed view in Figures 10(**b**), 10(**d**), 10(**f**), the dominant pitching frequency is slightly lower than the natural frequency St_n. Onoue et al. [7] reported a similar result and ascribed to the periodic formation of a leading edge vortex, which generates an aerodynamic torque, thereby reducing the effective stiffness and the effective natural frequency.

These results demonstrate a progressive transition from a flow-dominated regime to a fully-coupled aeroelastic regime, where frequency synchronization plays a key role in the establishment of limit-cycle oscillations.

5.4. Effect of Elastic Axis Position

The influence of the elastic axis location on the aeroelastic response is examined by comparing two configurations, corresponding to $X^*_{ec} = 0.50$ and $X^*_{ec} = 0.66$. The analysis focuses on the evolution of the oscillation amplitude as a function of reduced velocity.

As shown in Figure 11, the position of the elastic axis has a significant impact on the stability threshold of the system. In all cases, moving the elastic axis from $X^*_{ec} = 0.5$ (11(**a**), 11(**c**), 11(**e**)) to $X^*_{ec} = 0.66$ (Figures 11(**b**), 11(**d**), 11(**f**)) leads to an earlier onset of large-amplitude oscillations, corresponding to a lower critical reduced velocity.

This behaviour — particularly pronounced at $\alpha_0 = 0^\circ$ and gradually diminishing as the equilibrium angle of attack increases — can be attributed to the increase in the aerodynamic moment arm, which enhances the coupling between aerodynamic forces and structural motion. As a result, the system becomes more susceptible to instability. Despite this quantitative effect, the qualitative behaviour of the system remains unchanged. In particular, the nature of the transition observed for different equilibrium angles of attack is preserved. The subcritical behaviour at $\alpha_0 = 0^\circ$ and the supercritical behaviour at higher angles are observed for both elastic axis positions.

The frequency response (not shown) follows a similar trend, with the transition from vortex-shedding-dominated behaviour to synchronized aeroelastic motion occurring at lower values of reduced velocity when the elastic axis is located further downstream. These results indicate that the elastic axis position primarily affects the stability boundaries of the system, without altering the underlying mechanisms governing the aeroelastic response.

 doi:10.20944/preprints202605.1300.v1

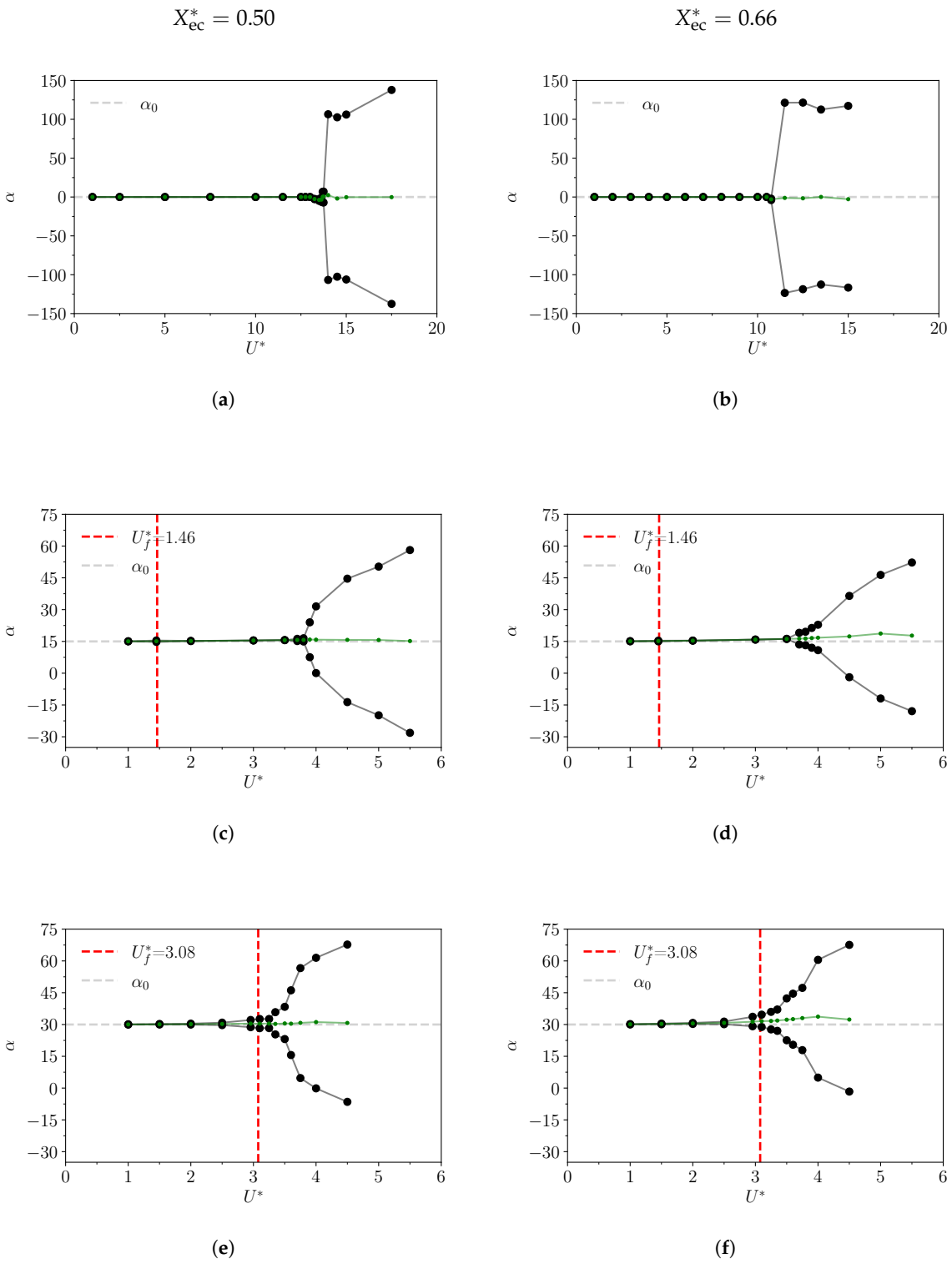

Figure 11. Maximum, minimum, and mean values of the angle of attack as a function of the reduced velocity U^* for two elastic-axis positions: $X^*_{ec} = 0.50$ (left column) and $X^*_{ec} = 0.66$ (right column), and for different equilibrium angles of attack: $\alpha_0 = 0°$ (top row), $\alpha_0 = 15°$ (middle row), and $\alpha_0 = 30°$ (bottom row). The gray dashed line indicates the equilibrium angle of attack, while the red dashed line denotes the reduced velocity corresponding to the Strouhal-number peak of the associated rigid-airfoil case. The black lines represent the maximum and minimum values of the angle of attack, and the green line denotes the mean value.

 doi:10.20944/preprints202605.1300.v1

6. Discussion

The aeroelastic response of a pitching NACA0012 airfoil at low Reynolds number has been investigated through a coupled fluid–structure numerical framework based on the Navier–Stokes equations in a rotating reference frame and a single-degree-of-freedom structural model.

The analysis of the rigid airfoil highlights three distinct flow regimes as the equilibrium angle of attack increases: a steady regime at low angle, a periodic vortex-shedding regime at intermediate angles, and a strongly nonlinear separated regime at high angles. These baseline behaviours provide a reference for interpreting the aeroelastic response of the coupled system.

When structural coupling is introduced, the system exhibits a transition from small-amplitude oscillations to large-amplitude limit-cycle oscillations as the reduced velocity increases. The nature of this transition depends on the equilibrium angle of attack. A subcritical bifurcation is observed at low angle of attack, where oscillations appear abruptly beyond a critical threshold, whereas a supercritical transition occurs at higher angles and is characterized by a gradual growth of the oscillation amplitude.

Frequency analysis reveals a progressive transition from a flow-dominated regime, governed by vortex shedding, to a fully coupled aeroelastic regime in which the motion is synchronized with the structural natural frequency. An intermediate regime is identified, in which both flow and structural time scales contribute to the system response.

The equilibrium angle of attack plays a key role in determining the onset of instability, with higher angles leading to earlier transitions and stronger aerodynamic forcing. The position of the elastic axis primarily affects the stability threshold, with downstream locations promoting an earlier onset of flutter, while the underlying bifurcation mechanisms remain unchanged.

Overall, the results demonstrate that stall flutter at low Reynolds number is governed by the interaction between vortex dynamics and structural response, and that both aerodynamic conditions and structural parameters strongly influence the stability boundaries and dynamical regimes of the system.

Author Contributions: Conceptualization, S.P., P.J. and G.S.; methodology, S.P., G.S. and M.A.C.; software, S.P. and G.S.; validation, G.S. and M.A.C.; investigation, S.P., G.S., P.J. and M.A.C.; data curation, G.S. and M.A.C.; writing—original draft preparation, M.A.C.; writing—review and editing, S.P., P.J. and G.S.; visualization, G.S. and M.A.C.; supervision, S.P. All authors have read and agreed to the published version of the manuscript.

Acknowledgments: We acknoledge that this research received financial support from ICSC-Centro Nazionale di Ricerca in 'High Performance Computing, Big Data and Quantum Computing', funded by European Union-NextGenerationEU. The results reported in this paper have been achieved using the EuroHPC Research Infrastructure resource LUMI supercomputer under project EHPC-REG-2025R02-307.

Conflicts of Interest: The authors declare no conflicts of interest.

References

1. European Union Aviation Safety Agency. Certification Specifications for Large Aeroplanes (CS-25), 2023. CS 25.629: Flutter, deformation, and failsafe criteria.
2. Menon, K.; Mittal, R. Flow physics and dynamics of flow-induced pitch oscillations of an airfoil. *Journal of Fluid Mechanics* **2019**, *877*, 582–613.
3. Lee, T.; Gerontakos, P. Investigation of flow over an oscillating airfoil. *Journal of Fluid Mechanics* **2004**, *512*, 313–341.
4. Kim, D.; Chang, J. Low-Reynolds-number effect on the aerodynamic characteristics of a pitching NACA0012 airfoil. *Aerospace Science and Technology* **2014**, *32*, 162–168.
5. Rezapour, S.; Mulleners, K. Dynamic stall reattachment revisited. *Journal of Fluid Mechanics* **2026**, *1029*, A52.
6. Poirel, D.; Harris, Y.; Benaissa, A. Self-sustained aeroelastic oscillations of a NACA0012 airfoil at low-to-moderate Reynolds numbers. *Journal of Fluids and Structures* **2008**, *24*, 700–719.
7. Onoue, K.; Song, A.; Strom, B.; Breuer, K. Large amplitude flow-induced oscillations and energy harvesting using a cyber-physical pitching plate. *Journal of Fluids and Structures* **2015**, *55*, 262–275.

 doi:10.20944/preprints202605.1300.v1

8. Qiu, Z.; Wang, F. Characterization of aeroelastic response and aerodynamic stiffness effect of an airfoil in the presence of dynamic stall. *Nonlinear Dynamics* **2023**, *111*, 129–154.
9. Xia, Y.; Dai, Y.; Huang, G.; Yang, C. Stall flutter mitigation of an airfoil by active surface morphing. *Physics of Fluids* **2024**, *36*.
10. Guo, J.; Dai, Y.; Huang, G.; Xi, Z.; Yang, C. Stall flutter prediction based on energy map by operator-network aerodynamic modeling. *AIAA Journal* **2025**, pp. 1–13.
11. Pirozzoli, S. Generalized conservative approximations of split convective derivative operators. *Journal of Computational Physics* **2010**, *229*, 7180–7190.
12. Pirozzoli, S. Stabilized non-dissipative approximations of Euler equations in generalized curvilinear coordinates. *J. Comput. Phys.* **2011**, *230*, 2997 – 3014.
13. Soldati, G.; Ceci, A.; Pirozzoli, S. FLEW: a DNS solver for compressible flows in generalized curvilinear coordinates. *Aerotecnica Missili & Spazio* **2024**, *103*, 413–425.
14. Dimitriadis, G.; Li, J. Bifurcation behavior of airfoil undergoing stall flutter oscillations in low-speed wind tunnel. *AIAA Journal* **2009**, *47*, 2577–2596.